Colloids and Surfaces A: Physicochemical and Engineering Aspects 629 (2021) 127391

Contents lists available at ScienceDirect

Colloids and Surfaces A: Physicochemical and Engineering Aspects

journal homepage: www.elsevier.com/locate/colsurfa

Interaction of vapor cloud and its effect on evaporation from microliter coaxial well

Digvijay Shukla, Pradipta K. Panigrahi *

Mechanical Engineering Department, Indian Institute of Technology Kanpur, Kanpur 208016, India

GRAPHICAL ABSTRACT

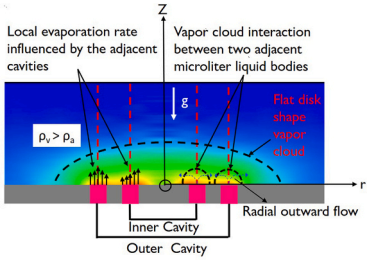

ARTICLE INFO

Keywords:
Evaporation
Digital holographic interferometry
Vapor cloud
Coaxial well

ABSTRACT

The evaporation of volatile heavy hydrocarbon liquid from coaxial well configuration is studied to understand the vapor phase transport, vapor cloud interaction and its effect on the local evaporation rate of two evaporating coaxial cavities of microliter volume. The gap between the two coaxial cavities is varied without varying the dimensions (width and depth) of the coaxial cavities for studying the vapor cloud interaction. Digital holographic Interferometry (DHI) is used to decipher the vapor mole fraction field above the coaxial well. Gravimetric measurement has been carried out for measuring the evaporation rate. Diffusion-limited simulation of evaporation process has been carried out using COMSOL Multiphysics software to understand the role of convective motion. IR thermography measurement of liquid interface temperature has been carried out to correlate the vapor cloud interaction with local evaporation rate and evaporation induced cooling. A flat-disk shaped vapor cloud surrounds the coaxial cavities. Total evaporation rate measured from DHI shows good agreement with the gravimetric measurement having maximum deviation of 3%. Good match between the evaporation rate measured from gravimetry and holography with diffusion limited model is observed at low Grashof number. The mismatch in evaporation rate with the diffusion limited model is observed at high Grashof number due to higher radius of the coaxial cavity indicating the dominance of convective motion. The evaporation rate from individual well decreases when liquid simultaneously evaporates from the inner and outer coaxial cavities. This reduction in evaporation rate increases with decrease in gap between the two coaxial cavities due to increase in interaction between the vapor cloud. The decrease in local evaporation rate from individual cavity due to presence of a neighboring evaporating cavity correlates with the evaporative cooling effect using temperature measurement of the interface from IR thermography. Vapor cloud interactions of microliter volume coaxial cavities can influence the evaporation rate of individual coaxial cavity and the convection inside the liquid phase. The present study demonstrates the capability to precisely control the evaporation process by appropriate design of coaxial well

* Corresponding author.
E-mail addresses: dvijay@iitk.ac.in (D. Shukla), panig@iitk.ac.in (P.K. Panigrahi).

https://doi.org/10.1016/j.colsurfa.2021.127391
Received 14 May 2021; Received in revised form 6 August 2021; Accepted 17 August 2021
Available online 25 August 2021

configuration. The results from the present study can be useful for controlling the evaporation rate in several applications i.e. protein crystal growth, DNA/RNA sequencing and microfabrication etc. by suitable design of coaxial well.

Nomenclature

C	molar concentration (mol/m^3)
C_p	specific heat (J/mol. K)
D	diffusion coefficient (m^2/s)
E	total evaporation rate (mg/s)
g	gravitational acceleration (m/s^2)
Gr	Grashof number
j	local evaporation rate (kg/s.m^2)
M	molecular weight (g/mol)
P	pressure (N/m^2)
Ru	universal gas constant (j/mol. K)
R	radius of coaxial cavity (mm)
t	time (s)
T	temperature (K)
r	radial co-ordinate
z	vertical co-ordinate
n	normal direction
x	horizontal co-ordinate
w	normalized width of cavity (mm)

Greek symbols

λ	wavelength of He-Ne laser (nm)
ϕ	phase shift (radian)
$\Delta\eta$	refractive index change
η	refractive index
χ	vapor mole fraction
ρ	density (kg/m^3)
μ	dynamic viscosity (kg/m.s)

Subscripts

a	air
v	vapor
σ	interface
mix	air-vapor mixture
ref	reference
amb	ambient
i	inner
o	outer
m	mean/mid plane
b	boiling
s	saturated
∞	far away from the surface

1. Introduction

Evaporation from reservoirs/wells has several applications such as microfluidic cell culture [1], protein/DNA microarray [2,3], micro reactors for chemical synthesis [4], point of care diagnostics and biological lab on chip devices, protein crystallization [5] etc. These miniaturized devices often contain chambers or reservoirs for storage and supply of fluid. The micro/nanoliter volume cavities/wells have an open liquid-air interface and evaporation from these cavities play a significant role in the functioning of the device. Uncontrolled evaporation from these microliters volume well cavities might cause significant liquid loss and reservoir dry out. This can eventually lead to the malfunctioning of the device. Walzl et al. [6] observed that the uneven loss of growth medium due to unequal evaporation in cellular screening assays depending on the microwell position influences the readout of cellular metabolic activity. The control of evaporation from the cavity can influence the performance of these devices. For example, the quality of protein crystal depends on the rate of evaporation from the droplet containing protein solution to the surrounding reservoir well [7]. Control of evaporation also influences the deposition pattern [8–12] and micro handling of DNA array [6] etc. Pradhan and Panigrahi reported the evaporation induced natural convection inside a droplet of aqueous solution placed on a superhydrophobic surface [13].

Chen et al. [8,14] studied evaporation of volatile liquid droplet in a circular well with flat wall. They observed that it is possible to control the deposition pattern by adjusting the dimension of well. Lynn et al. [15] studied the evolution of meniscus shape using a two-step method for estimation of the instantaneous evaporation rate of water evaporating from contracting and expanding circular micro reservoirs. They observed that evaporation is enhanced in expanding reservoir and suppressed in contracting reservoir. Shukla and Panigrahi [16] studied the evaporation from a circular well cavity of small depth. Their study on evaporation of heavy hydrocarbons from a circular cavity revealed the presence of natural convection in the vapor cloud which influences the shape of the vapor cloud compared to the pure diffusion model.

Walzl et al. [6] observed that uneven loss of growth medium in cellular screening experiments depend upon the position of microwell on the plate (edge, corner and center) due to the influence on evaporation characteristics of individual well. The vapor cloud interaction can lead to change in concentration gradient leading to variation in evaporation rate distribution and internal convection inside the liquid phase. For example, suppression of internal convection inside a droplet in the presence of another liquid coaxial reservoir can affect the protein crystallization process [7]. Mixing of analyte and reaction time can also be affected by change in evaporation rate of a well due to the presence of another well which can affect the behavior of several processes i.e. DNA/RNA sequencing, microchemical rectors, microfabrication etc. Uniform deposition can be achieved by controlling the evaporation rate distribution which is important in several applications like organic light emitting diode (OLED) fabrication, pattern direct writing of color filter, inkjet printing etc. The present study proposes a multiple microliter volume coaxial well design, where evaporation rate of individual cavities is influenced by the interaction between vapor cloud.

Few studies have reported the vapor cloud interaction in droplet geometries. Pradhan and Panigrahi [17] studied the influence of an adjacent droplet on liquid convection inside an evaporating droplet of binary mixture. The presence of an adjacent droplet leads to asymmetric evaporative flux distribution on the droplet surface due to the change in free stream mass fraction by the evaporation from the neighboring droplet. Pradhan and Panigrahi [18] also reported the effect of a neighboring liquid droplet on fluid convection inside a droplet of aqueous solution, which were located physically apart and had different solute concentrations. Vapor mediated interaction of two condensing droplets influences the internal flow structure which changes from symmetric for single droplet case to asymmetric for two condensing droplet case [19]. Recently, Wen et al. [20] reported the motion of two pure liquid droplets placed on a high energy substrate and attributed the motion to the gradient in the liquid vapor concentration resulting from

evaporation. Droplet movement was observed from higher evaporation side to the lower evaporation side.

The study of vapor distribution surrounding the coaxial cavities is another example of vapor cloud interaction due to the evaporation of adjacent liquid bodies/droplets. The interaction of vapor cloud from the two coaxial well cavities can explain how vapor mole fraction distribution affects the vapor mole fraction gradient at the interface so as evaporation phenomena. The quantitative estimation of vapor mole fraction distribution can help in understanding the coupled diffusion, convection, and evaporation process. Planar laser induced fluorescence (PLIF) [21,22] and Fourier transform infrared spectrometry (FTIR) [23] have been previously used for vapor concentration measurement. The limitation of these techniques is poor accuracy in measurement in the vicinity of the evaporating liquid interface. Holographic interferometry is another technique for accurate measurement of the vapor mole fraction and concentration gradient at the interface. Interferometry has been used for vapor cloud studies in droplet geometries [24,25]. Dehaeck et al. [26] experimentally measured local evaporation rate and interfacial temperature of a suspended HFE-7100 droplet by using digital holographic interferometry technique. The experimentally measured vapor cloud differs from the steady-state diffusion-limited model. Most of the studies of evaporation of droplet have been carried out for the fluids whose vapor is lighter than the surrounding medium and diffusion was reported to be the main mechanism inside the vapor cloud [27]. Only a handful number of studies were performed for the fluids which are heavier than the surrounding medium i.e., pentane, hexane etc. These studies revealed the presence of buoyancy induced natural convection in the vapor phase and experimentally obtained evaporation rates are always higher compared to the conventional steady-state diffusion model [16,26,28,29].

The literature review on evaporation of adjacent micro litter volume liquid droplet has shown the role played by the interaction between the vapor cloud. However, to the best of our knowledge, no detailed study on vapor cloud interaction due to evaporation of more than one micro litter well cavity/droplet has been reported in literature compared to the internal flow measurements reported in various previous studies [17–19]. In the present study, vapor phase transport and vapor cloud interactions of microliter volume coaxial cavities are studied by digital holographic interferometry. Gravimetric analysis has been performed to measure the evaporation rate. Simulation study using diffusion limited model has been carried out to explain the transport process inside the vapor cloud. Temporal and spatial behavior of vapor cloud originating from coaxial cavities and their mutual interactions are discussed. Effect of vapor cloud interaction on global and local evaporation rate from the coaxial cavities has been reported. The depth and width of the cavities are kept constant while gap between the two cavities is varied to study the effect of vapor cloud interaction on the vapor mole fraction distribution. Overall, the present study successfully demonstrates the vapor cloud interaction behavior of evaporating microliter well. It demonstrates the potential of controlled evaporation using coaxial cavity configuration, which has potential application in several devices/systems.

2. Experimental details

The experimental details are presented below as per the following sequence: (a) Experimental configuration, (b) Gravimetric measurement, (c) Digital holography interferometry, (d) Data analysis and (e) Simulation of diffusive transport.

2.1. Experimental configuration

Fig. 1 shows the schematic of the coaxial well geometry used for study of evaporation process. Coaxial wells are made from plexiglass material and pasted on a glass slide with the help of epoxy glue. The cavities are 1 mm wide and 2 mm deep. The radial distance from the center of the cavity and the gap between the annular cavities are different in two coaxial well configurations. The distance of the inner cavity from the absolute center is 1.5 mm for coaxial well-1 and 1 mm for coaxial well-2. The gap between the two cavities is equal to 1 mm for coaxial well-1 and equal to 0.5 mm for coaxial well-2. Hexane is used as working fluid. Table 1 shows the physical properties of hexane. Evaporation occurs at ambient condition due to the low saturation pressure of hexane causing significant change in refractive index in the gas vapor

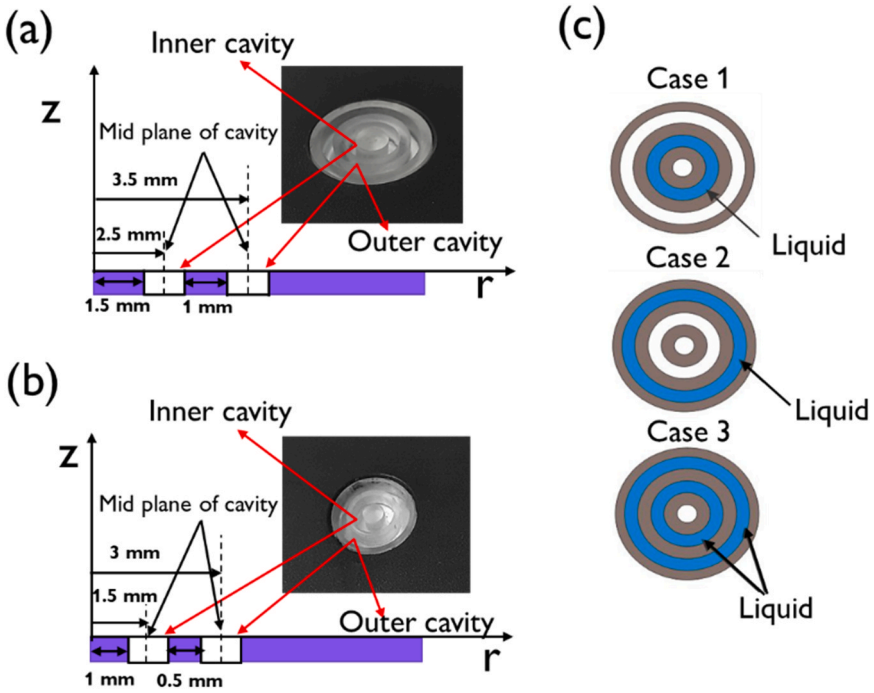

Fig. 1. Schematic and geometric details of coaxial well cavity: (a) Coaxial well-1, (b) Coaxial well-2 (the photograph is shown as inserts) and (c) Pictorial view of different test cases (1–3).

Table 1
Thermo-physical properties of hexane at 25 °C. Molecular weight (M), boiling point (T_b) and specific heat (C_p) values are adopted from [30]. Diffusivity (D) values are taken from ref [31]. Vapor pressure (P_v) is obtained from using Antoine equation [32].

Fluid	M (g/mol)	P_v (kPa)	T_b (°C)	D (m^2/s) × 10^{-6}	C_P (J/mol. K)
Hexane (C_6H_{14})	86.174	20.265	68.5	8.2	197.66

mixture above the evaporating liquid. The experiments for each coaxial well have been carried out in three different configurations. Pictorial view of these cases is shown in Fig. 1(c). In the first case (case-1), only the inner cavity is filled. In the second case (case-2), the outer coaxial cavity is filled. In the third case (case-3), both inner and outer cavities are filled simultaneously. The experiments are carried out 3 times for each case. Repeatability of the experiments is assured by comparing the different data sets for the same experimental condition.

2.2. Gravimetric measurement

Evaporation rate of the coaxial well has been measured by gravimetric approach. A precision electronic balance (OHAUS Adventurer AVG 264 C) with a resolution of 0.1 mg is used for recording the mass loss due to evaporation from the coaxial well with time. The impulse generated during pouring the liquid inside the coaxial well cavities may affect the measurement at the initial period. Therefore, the measurements during the initial period are not considered for evaporation rate calculation. A linear fit between mass and time data is performed over a range of 90–50% of the initial mass and negative of its slope is taken as an evaporation rate. The value of regression co-efficient lies above 0.99 for this range of data. More details on the gravimetric measurements can be found in [16].

2.3. Digital holography interferometry

An off-axis digital holographic setup with wedge fringe setting mode is used for mole fraction distribution measurement over the well. The layout of the off-axis digital holography setup is shown in Fig. 2(a). The collimated beam of wavelength 632.8 nm from He-Ne laser is divided into two beams (object and reference) with the help of beam splitters and plane mirrors. The object beam passes through the vapor cloud above the coaxial well cavity, while the reference beam of equal path length passes through the ambient air. Vapor cloud of hexane vapor due to evaporation from coaxial cavity, causes a change in the refractive index above the coaxial well. It generates an optical path difference between the object and reference beam. The resulting interference pattern due to the superposition of object and reference beam is recorded on a CCD camera which is known as a hologram. More details on the experimental arrangement are available in [16].

Before filling the liquid inside the coaxial cavities, a reference hologram is recorded. The liquid is filled inside the coaxial well and several holograms are recorded at the time interval of 250 ms.

2.4. Data analysis

A Fourier Transform Profilometry [33] algorithm is used to extract the phase from the recorded object holograms. The phase obtained from each object hologram is subtracted from the phase of reference hologram. This extracted phase is called as wrapped phase because actual phase values are wrapped between $-\pi$ to $+\pi$, due to the use of arctan function in the phase extraction algorithm. This 2π phase discontinuity in the wrapped phase is removed by Goldstein algorithm [34]. The resulted phase distribution is called the unwrapped phase (Φ). The obtained unwrapped phase is projected phase difference for each line of sight, perpendicular to the direction of propagation of laser beam. Hence, the unwrapped phase needs to be tomographically reconstructed to yield a three-dimensional refractive index change field. Since, the refractive index field around liquid evaporating from a coaxial well cavities is axisymmetric in nature (as experiments are performed in the quiescent environment in the closed room), the refractive index field can be obtained by inverse Abel inversion of unwrapped phase [35–37]. The change in refractive index, Δn at any height, z is given by the following equation:

$$\Delta\eta(r) = \frac{-\lambda}{2\pi^2}\int_r^\infty \frac{\phi'(x)}{\sqrt{x^2 - r^2}}dx \quad (1)$$

Here, $\Delta\eta = (\eta_{mix} - \eta_a)$, η_{mix} denotes the refractive index of air-vapor mixture, n_a is the refractive index of pure air at ambient temperature and pressure, r is the radial co-ordinate, λ is the wavelength of laser beam and $\phi'(x)$ is the first derivative of the unwrapped phase shift. Co-ordinate system used is shown in Fig. 2(b). Fourier-Henkel algorithm is used to perform Abel inversion [36].

Fig. 3(a) shows a sample raw object hologram of hexane vapor evaporating from the inner coaxial cavity. Fig. 3(b) shows the corresponding unwrapped phase distribution obtained after implementing the Goldstein algorithm. The 3D refractive index field obtained using the Abel Inversion algorithm is shown in Fig. 3(c). The vapor mole fraction field, χ can be obtained from the refractive index field by Lorentz-Lorenz equation [38,39]. The following equation describes the relationship of mole fraction, χ with the refractive index difference and local temperature T [26].

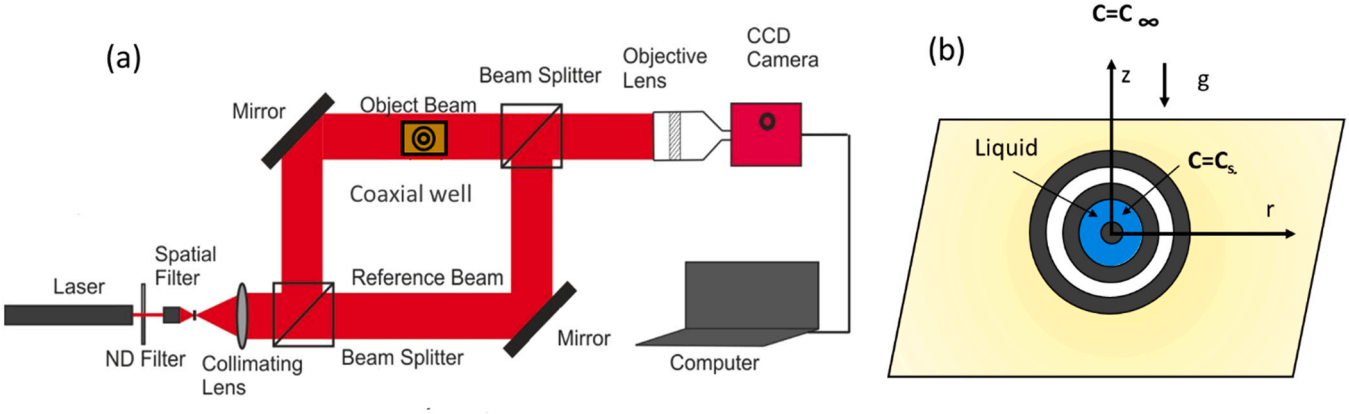

Fig. 2. (a) Schematic of the off-axis digital holography setup and (b) the sketch representing the coordinate system of the coaxial well cavity.

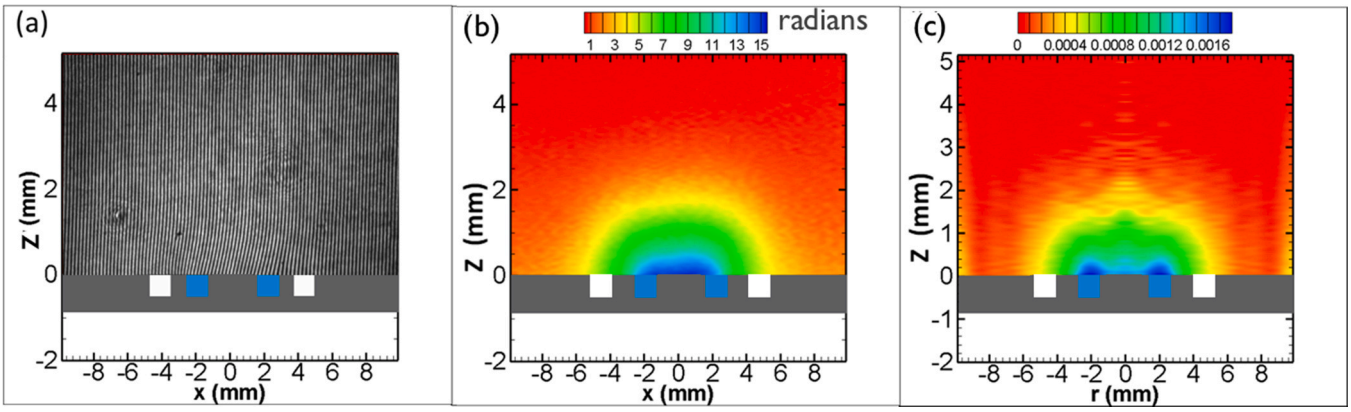

Fig. 3. Different stages of holographic data analysis: (a) raw object hologram, (b) unwrapped phase map and (c) refractive index field after Abel inversion.

$$\chi = \frac{1}{\Delta\eta_{ref}} \frac{T}{T_{amb}} \left[\Delta\eta - (\eta_a - 1)\left(\frac{T_{amb}}{T} - 1 \right) \right] \tag{2}$$

Where, $\Delta\eta_{ref} = (\eta_v - \eta_a)$, η_v and η_a are the refractive index of pure vapor of liquid and air respectively at ambient temperature and pressure. If the temperature difference is marginal, then by setting, $T \approx T_{amb}$ [26], the vapor mole fraction can be computed using the following expression:

$$\chi = \frac{\Delta\eta}{\Delta\eta_{ref}} \tag{3}$$

The values of n_v and n_a at wavelength of 632.8 nm is equal to 1.00183 and 1.0002679 respectively [40]. The normal gradient, $\partial\chi/\partial n$ can be extracted at the liquid-vapor interface from the vapor mole fraction field obtained from digital holographic interferometry. Local evaporation rate, j(r) at the liquid-vapor interface can be calculated by using the normal mole fraction gradient in the following equation [26]:

$$j(r) = -\frac{M_v P_{amb} D}{R_u T_{amb}(1-\chi_\sigma)} \frac{\partial\chi(r,z)}{\partial n} \tag{4}$$

Here, M_v (86 g/mol) is the molecular weight of vapor, P_{amb} (101.325 kpa) is the total atmospheric pressure, T_{amb} (298.15 K) is the ambient temperature, χ_σ is the mole fraction at the interface, R_u (8.3145 j/mol.K) is the universal gas constant and $\frac{\partial\chi}{\partial n}$ is the gradient of mole fraction at the interface. Global evaporation rate, E can be calculated by integrating the local evaporation rate over the cavity surface area, s as:

$$E = \int_\sigma j(r) ds \tag{5}$$

2.5. Simulation of diffusive transport

The evaporation rate from the well can be obtained assuming steady state diffusion. The diffusion - convection equation reduces to the Laplace equation for the concentration field C (r, z) as:

$$\frac{1}{r}\frac{\partial}{\partial r}\left(r\frac{\partial C}{\partial r} \right) + \frac{\partial^2 C}{\partial z^2} = 0 \tag{6}$$

Eq. (6) can be solved to yield the vapor concentration field above the coaxial well using following boundary conditions (see Fig. 2(b)):

$C = C_s$; at $R_i < r > R_o$ and $z = 0$

$C = C_\infty$ at $r, z \to \infty$

Here, R_i and R_o are the inner and outer radius of the respective coaxial cavity filled with hexane, C_s is the saturated concentration of vapor at ambient temperature and C_∞ is the concentration of vapor present in ambient air. The value of C_s is equal to 8.17 mol/m^3 at temperature of 25 °C while C_∞ is equal to 0 since the hexane vapor is absent in ambient air. The liquid vapor interface is assumed to be flat. The local evaporation flux at the liquid-vapor interface can be calculated using Fick's law as:

$$j(r) = -D\frac{\partial C(r,z)}{\partial z} \tag{7}$$

Where, D is the diffusion co-efficient of vapor in air and concentration gradient is taken at the liquid-vapor interface, i.e. z = 0. The global evaporation rate can be calculated by integrating the local evaporation rate over the coaxial cavity interface as shown in Eq. (5).

Eq. (6) is numerically solved in COMSOL Multiphysics software to yield the vapor concentration field inside the vapor cloud. Local and total evaporation fluxes are calculated using Eqs. (7) and (5) respectively. The simulation was first validated for the flat circular disk (weber disk), by comparing the local, j(r) and total evaporation rate, E from the present simulation with the analytical expression [41]:

$$j(r) = \frac{2}{\pi}\frac{D(C_s - C_\infty)}{\sqrt{R^2 - r^2}} \tag{8}$$

$$E = 4DR(C_S - C_\infty) \tag{9}$$

A 1.5 mm radius disk filled with hexane is considered and saturated vapor concentration boundary condition ($C_s = 8.17$ mol/m^3) is applied at the interface. The computational domain size is taken as 30 times larger than the disk radius with boundary condition $C_\infty = 0$ as no vapor is present in the ambient. Schematic diagram of the computational domain and boundary conditions is shown in Fig. 4(a). A linear grid refinement is applied at the interface region to properly resolve the concentration gradient at the interface (see Fig. 4(a)). The interface region is discretised with 3000 number of elements. Grid independence is checked by varying the no of elements at the interface from 3000 to 4000 and the difference obtained in the total evaporation rate is 0.3%. The local evaporation rate is compared with the analytical evaporation rate as shown in Fig. 4(b). The maximum difference between the total evaporation rate from numerical simulation and analytical expression is only 0.28%. After successful validation of simulation for flat circular disk, simulation of evaporation for coaxial cavity configuration was carried out.

2.6. Uncertainty analysis

The error in evaporation rate obtained from gravimetric measurement can be attributed to the micropipette setting error of initial volume of liquid, resolution of the electronic balance and fluctuation in ambient conditions. Experiments are repeated at least three times and the average values from the multiple experiments are reported. The

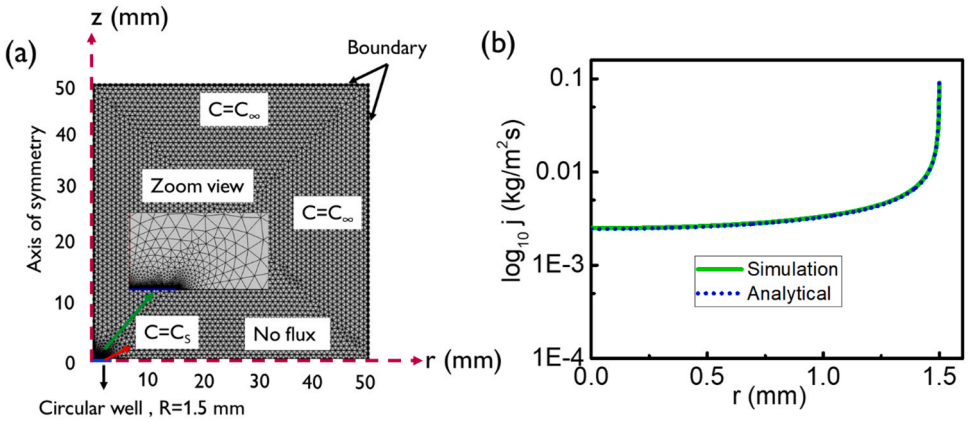

Fig. 4. (a) Schematic diagram of computational domain and boundary conditions and (b) Comparison of numerical and analytical local evaporation rate distribution (j) for the circular flat disk of 1.5 mm radius.

electronic balance used for gravimetric measurement is set to zero value at the beginning of each experiment. Therefore, bias error is insignificant in the evaporation rate measurement. The least count of the electronic balance is equal to 0.1 mg. Maximum uncertainty of evaporation rate from gravimetry is equal to 6%. Any bias error due to electronic noise or other environmental effects are eliminated during holographic data inversion by subtracting the reference intensity image from the object field image. Holographic interferogram pattern can also be influenced by the error in the initial volume of liquid inside the coaxial cavity, convection inside the room, fluctuation of the incident light, and image acquisition error. Similar holographic interferograms were observed in repeated experiments. The maximum uncertainty in the intensity value of the interferogram is observed to be equal to 5%. The uncertainty in vapor mole fraction distribution can be attributed to the various factors such as fluctuation in intensity distribution, error propagation due to phase unwrapping, and tomographic inversion. The maximum uncertainty in vapor mole fraction distribution from repeated measurements is observed to be equal to 4%. The uncertainty estimated for evaporation rate calculation from holography measurement is equal to 5%.

3. Results and discussions

The vapor cloud characteristics above the evaporating liquid from the coaxial well is a manifestation of evaporation process and vice versa. The evaporation flux from neighboring wells in coaxial well configuration interacts with each other. The strength of interaction depends on the radial separation distance between the evaporating interface and the relative evaporation rate. The evaporation rate depends on the liquid interface area. The parametric influence of these factors has been investigated using two coaxial well configurations (See Fig. 1(a, b)). The experiments in each coaxial well configuration are carried out for three different test cases i.e., by filling up the liquid in the inner cavity, outer cavity, and both (See Fig. 1(c)). The results are presented and discussed in the following sequence: (a) Vapor concentration distribution, (b) Spatial and temporal behavior of vapor mole fraction profile, (c) Total evaporation rate, (d) Local evaporation rate and diffusive transport, and (e) Interface temperature.

3.1. Vapor concentration distribution

Fig. 5 shows the interferogram i.e. wrapped phase map during the initial time period (t = 0 + (s)) for coaxial well-1 and coaxial well-2 for

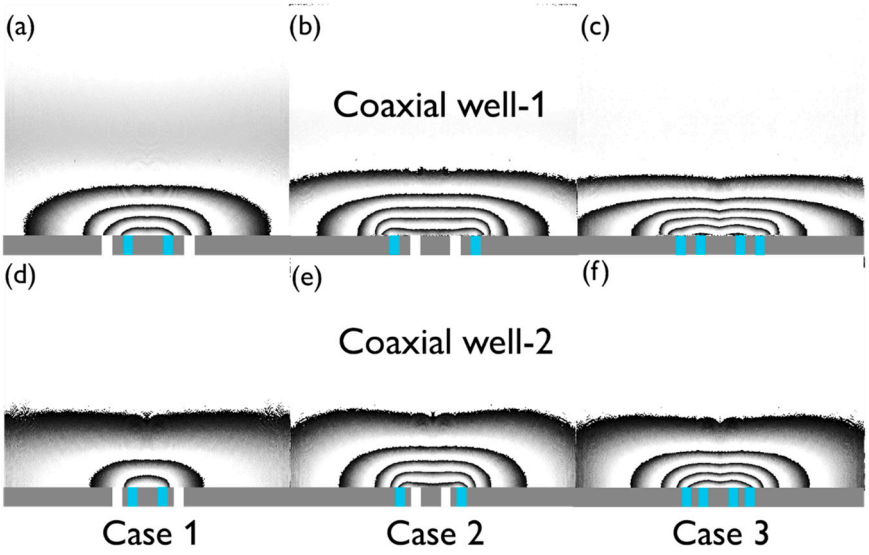

Fig. 5. Interferogram (Iso-concentration contours) at initial time t = 0 + (s) for different test cases of coaxial well-1 (a–c) and coaxial well- 2 (d–f). The schematic of the coaxial well test cases is shown inside the figure. Here, blue represents the cavities filled with liquid and white color represents empty cavity. (For interpretation of the references to color in this figure legend, the reader is referred to the web version of this article.)

different test cases (Case 1, 2 and 3). The fringes represent the iso-concentration contour of hexane vapor cloud. Iso-concentration lines are flat disked shaped instead of hemispherical as in case of pure steady diffusion [16,23]. This might be attributed to the fact that hexane vapor is almost three times heavier than surrounding medium (air). This restricts the vapor cloud movement in upward direction and there is radial transport of vapor evaporating from the well. The number of fringes for case-1 with filled inner cavity for coaxial well-1 is higher than that of coaxial well-2. Both the radial extent and axial extent of vapor cloud for coaxial well-1 is higher than that of coaxial well-2. This may be attributed to higher radius of inner cavity for coaxial well-1 compared to that of coaxial well-2 leading to higher interfacial area and thus higher rate of evaporation. The case-2 corresponds to the filling of working fluid in outer cavity. The number of fringes for Case-2 is higher than that of Case-1. This is attributed to higher evaporation of Case-2 compared to that of Case-1 due to longer interfacial area of the outer cavity compared to the inner cavity. The fringe near the liquid interface for Case-2 shows a lift-off due to the evaporation flux. The number of fringes in Case-3 i.e., when liquid is filled in both inner and outer cavity is not different from that of Case-2 i.e., when the liquid is filled in outer cavity only. This indicates insignificant change in total evaporation rate for Case-3 with respect to Case-2. However, the curvature of the fringe near the cavity in Case-3 shows distinct difference compared to that of Case-2. This may be attributed to the interaction between the vapor cloud of inner cavity with that of outer cavity. This interaction behavior between the vapor cloud will be discussed in the following section.

Fig. 6. shows the normalized mole fraction distribution on the substrate surface (z = 0) for both coaxial well configurations. Comparison of Fig. 6(a) for coaxial well-1 with Fig. 6(b) for coaxial well-2 shows greater spreading in mole fraction distribution of the former than later due to higher radius of the cavity for the former. Comparison between Fig. 6(a) and (c) for coaxial well-1 shows higher radial spreading when the outer cavity is filled with the working fluid (Case-2) compared to when fluid is filled in inner cavity. The vapor cloud from the evaporation of outer cavity fills up the inner cavity, which can be observed from the higher concentration of vapor mole fraction inside the inner cavity in Fig. 6(c). Comparison of Fig. 6(c) with (d) for coaxial well-2 shows overall increase in vapor concentration in the inner region is higher for coaxial well-1 than coaxial well-2 due to presumably higher evaporation rate for the former case. Fig. 6(e) and (f) show the mole fraction distribution for Case-3 i.e. when both the inner and outer cavity are filled with hexane. Fig. 6(e) shows higher vapor mole fraction in the gap region between the inner and outer cavity compared to the center region of the coaxial well. This may be attributed to the combined influence from the inner and outer cavity. The vapor mole fraction distribution in the gap region between outer and inner cavity for coaxial well-2 does not show dual peak behavior possibly due to smaller gap between inner and outer cavity for coaxial well-2 (see Fig. 6(e)). Overall, Fig. 6 indicates the role played by the vapor cloud interaction between the inner and outer cavity on the overall evaporation process.

The vertical plane vapor mole fraction distribution of hexane evaporating from the coaxial wells at initial time period (t = 0 + (s)) for different cases are presented in Fig. 7. The saturated vapor mole fraction at the liquid vapor interface at the ambient temperature of 25 °C is equal to 0.2. The vapor mole fraction at the top surface of liquid-air interface is equal to vapor mole fraction at the liquid-vapor interface. The vapor mole fraction changes in both transverse and radial direction due to the mass transfer from the higher mole fraction region to the ambient region i.e. ($C_\infty = 0$). The transverse extent of vapor cloud is lower than the radial extent as the hexane vapor is heavier than the ambient air and the heavier vapor moves downward and spread radially outward. The vapor mole fraction at the center region of case-1, coaxial well-2 in Fig. 7(d) can not be clearly distinguished from the inner cavity region contrary to that of coaxial well-1 (Fig. 7(a)) due to smaller inner radius. Similarly, the four peaks of vapor mole fraction observed in Fig. 7(e) for coaxial well-1 is not observed in Fig. 7(f) for coaxial well-2 due to lower gap

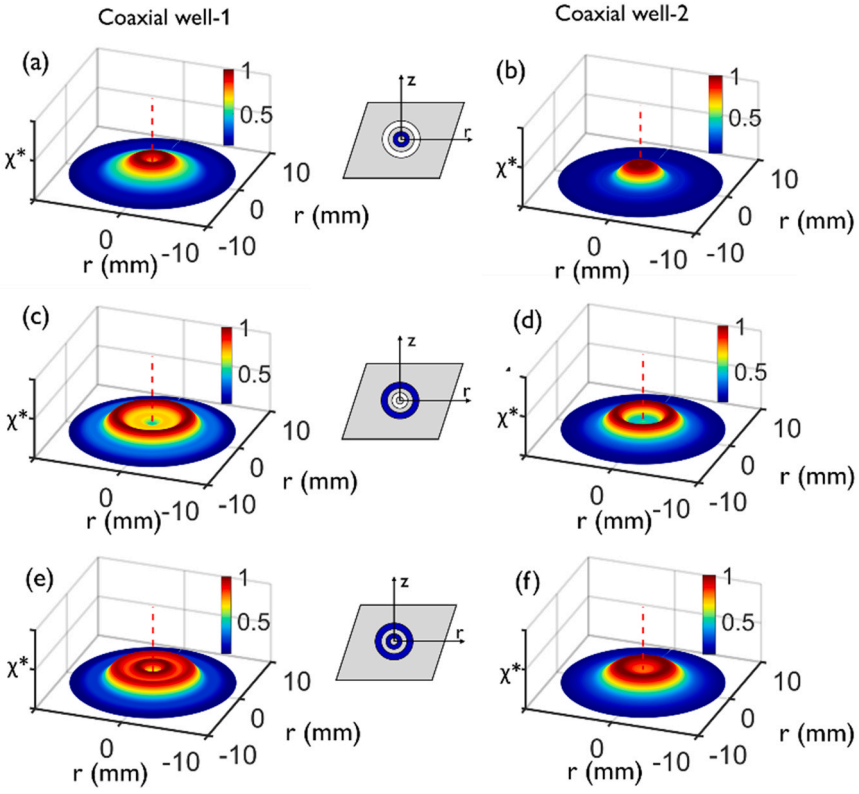

Fig. 6. Surface plots of normalized radial vapor mole fraction distribution ($\chi^* = \chi/\chi_{max}$) at the liquid vapor interface (z = 0 μm) during initial time period, t = 0 + (s) for different test cases: Coaxial well-1; (a) case-1, (c) case-2 and (e) case-3 and coaxial well-2; (b) case-1, (d) case-2 and (c) case-3.

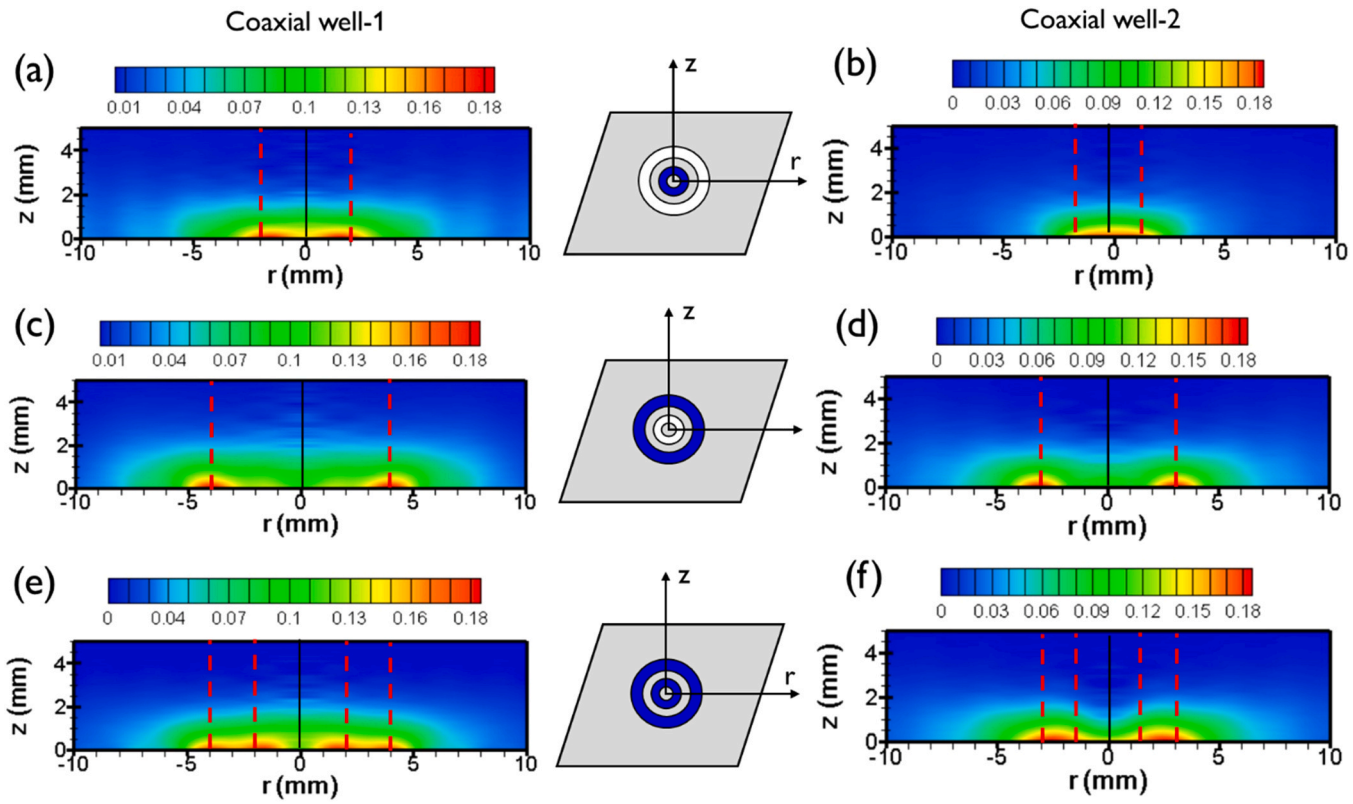

Fig. 7. Vapor cloud mole fraction contour of hexane evaporating from coaxial cavities at the initial time period (t = 0 + (s)): Coaxial well-1; (a) case-1, (b) case-2 and (c) case-3 and coaxial well-2; (d) case-1, (e) case-2 and (f) case-3.

between the inner and outer cavity.

Vapor mole fraction map indicates that a vapor plume emerges from the cavity and then it diffuses in the normal direction along with the combined convective and diffusive transport in radial direction. Thickness of vapor cloud is similar for both well configurations in all test cases. This indicate that vapor layer thickness in transverse direction does not show strong dependence with the size and gap of the coaxial cavities. However, the overall transverse shape of the vapor cloud in case-3 (Fig. 7(e) and (f)) is different between coaxial well-1 and coaxial well-2 due to interaction of evaporation from inner and outer cavity. In case-1, where the liquid is evaporated only from the inner cavity, a distinct immerging plume can be seen in coaxial well-1, where the distance from the absolute center is large compared to the coaxial well-2. In coaxial well-2, accumulation of vapor can be seen between the absolute center and inner edge of the cavity due to small radius of the inner cavity. Evaporation from outer cavities in both the configurations shows similar behavior, where the plume emerges from the cavity and spreads towards the edges. The plume is symmetric from the midplane of the cavity. In case-3, the interaction of the vapor plume is different in co-axial well-1 and 2. Two distinct plumes emerging from the inner and outer cavities can be seen in coaxial well-1, which eventually merges with each other. In coaxial well-2 plumes from inner and outer cavity completely merge and forms a single plume. This behavior is similar to the motion of two pure droplet on a high energy substrate due to gradient in vapor mole fraction as suggested by Wen et al [20]. This change in vapor mole fraction distribution may affect the internal motion of fluid and different nature of internal motion is expected in both configurations [17]. So, the evaporation rate of the coaxial cavities can be influenced by changing the gap between the cavities. There will be change in local evaporation rate distribution and interfacial temperature of the liquid interface. As a result, the internal convection inside the fluid can influence the deposition pattern inside the well. The deposition process can influence the performance of DNA/RNA stretching and manufacturing of OLED displays etc. The convective flow in the gas phase can cause a shear stress at the interface and influence the internal convection inside liquid. Thus, detailed spatial and temporal characteristics of vapor mole fraction distribution from the coaxial cavities are discussed in the following section.

3.2. *Temporal behavior of vapor mole fraction profiles*

Radial vapor mole fraction profiles at various vertical elevations from the top surface of the coaxial wells for different test cases at initial time period, t = 0 + (s) are shown in Fig. 8. The location of midplane of the inner and outer cavity is indicated by the dotted line in both well configurations. Fig. 8(a) shows the peak vapor mole fraction value is same for case-1 and case-2 for coaxial well-1 indicating same local evaporation rate for both inner and outer cavity. Comparison of Fig. 8 (a–d) show drop in peak vapor mole fraction value in the transverse (z) direction. A smaller peak is observed near the outer cavity (r = 4 mm) for case-1 and near the inner cavity (r = 2 mm) for case-2. This dual peak behavior is attributed to the accumulation of the vapor from the evaporating cavity inside the empty cavity. Fig. 8(a–d) shows dual peak in vapor mole fraction due to evaporation from both inner and outer cavity for case 3 of coaxial well-1. The magnitude of both the peaks reduces in transverse (z) direction. However, the reduction in peak is higher for the outer cavity compared to the inner cavity. This behavior is attributed to the influence of vapor cloud interaction from the inner cavity and outer cavity.

Fig. 8(e–h) shows similar unimodal vapor mole fraction for case-1 and case-2 of coaxial well-2 evaporation case. However, the nature of profile is different from that of coaxial well-1. The vapor mole fraction is more uniform in the central region of coaxial well-2 compared to that of co-axial well-1 for case-1. In case-2, the second peak of vapor mole fraction in the adjacent empty cavity region is absent for coaxial well-2. A dip in vapor mole fraction is observed in the empty cavity region. This

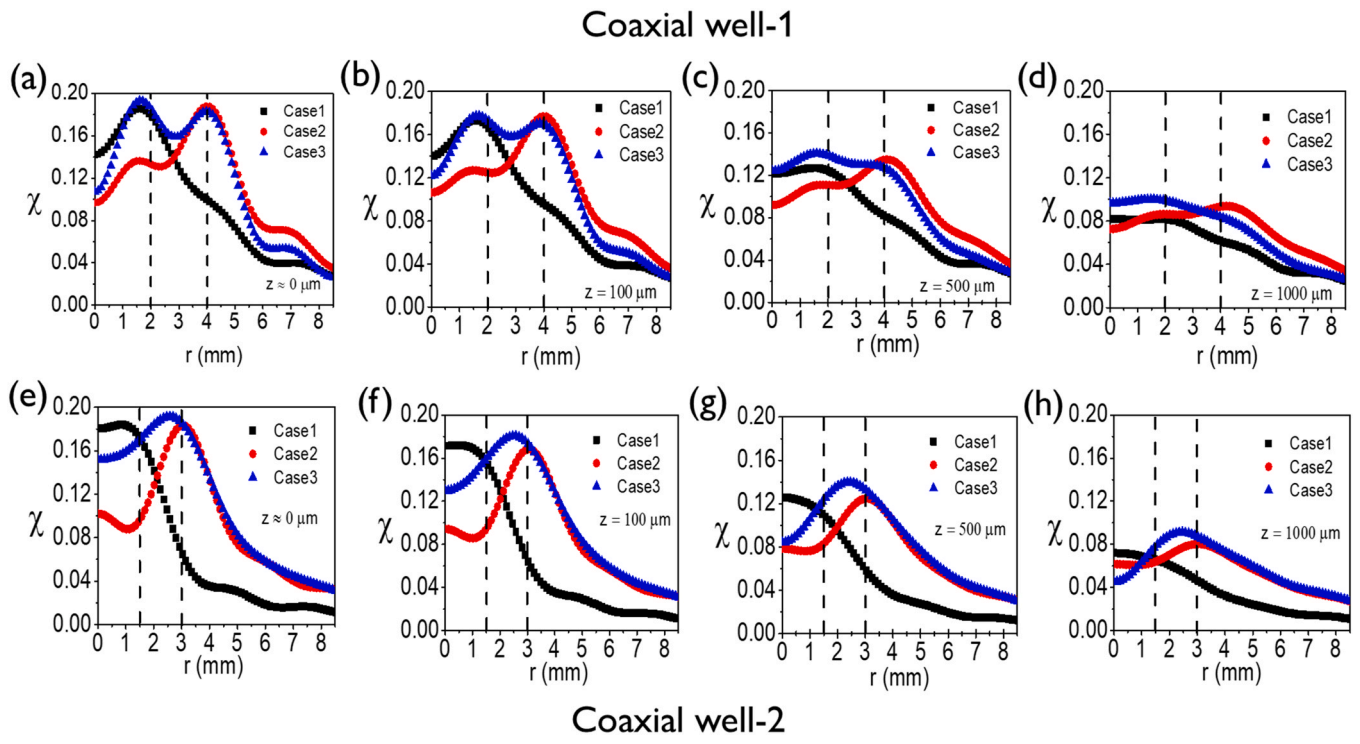

Fig. 8. Vapor mole fraction distribution in radial direction at initial time period t = 0 + (s) at various normal distance (z) from the top surface of the coaxial cavity: Coaxial well-1 (a–d) and Coaxial well-2 (e–h).

may be attributed to the initial filling up time of vapor cloud inside the cavity. The dual peak of vapor mole fraction is not seen for case-3 of coaxial well-2 contrary to that of coaxial well-1. This may be attributed to greater interaction between the vapor cloud for coaxial well-2 due to smaller gap. One interesting observation is that the peak mole fraction value in inner cavity for case-3 is lower than that of case-1. This indicates that the presence of a secondary coaxial cavity influences the evaporation from a coaxial cavity. Hence, the evaporation from a coaxial well can be controlled by introducing additional cavity and varying the relative radial distance between the cavities. Overall, Fig. 8 demonstrates significant influence of coaxial well design on the vapor mole fraction distribution.

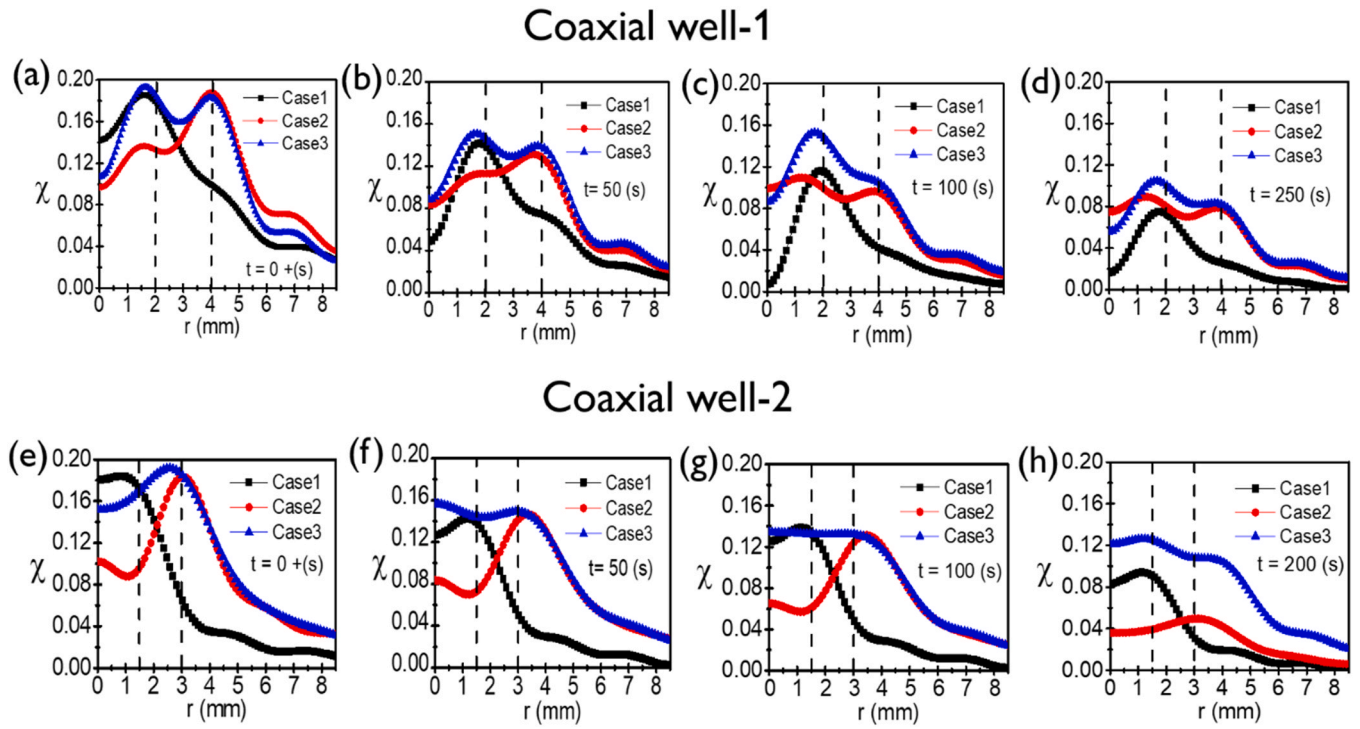

Fig. 9. Temporal variation of vapor mole fraction profile in the radial direction at the top surface of the cavity (z ≈ 0) for different test cases (Case 1, 2 and 3): Coaxial well-1 (a–d) and Coaxial well-2 (e–h).

Temporal variation of radial vapor mole fraction distribution at the top surface of coaxial cavity ($z \approx 0$) for both well configurations is presented in Fig. 9. Midplane of the coaxial cavities is shown by a dotted line. The nature of radial mole fraction distribution remains same with time for case-1 i.e. for inner cavity filled with hexane for both coaxial well-1 and coaxial well-2. Only the magnitude of vapor mole fraction reduces indicating reduced evaporation rate with time. Dual peak of vapor mole fraction is observed for case-2 i.e. outer filled cavity for coaxial well-1. In the beginning time period ($t < 100$ s), higher vapor mole fraction is observed for outer cavity compared to the inner cavity. However, at later time ($t > 100$ s) the drop in peak of vapor mole fraction is higher in the outer cavity region. At $t = 250$ s, the dual peaks have similar magnitude. It may be noted that the dual peak is attributed to the accumulation of the vapor cloud in the inner cavity region from evaporation of the outer cavity filled with hexane. The dual peak in case-3 for coaxial well-1 configurations drops with time. The drop in peak magnitude for the outer cavity is higher compared to that of the inner cavity. This may be attributed to the higher radial mass transfer from the outer vapor cloud. The vapor mole fraction profile for coaxial well-2 is different from that of coaxial well-1 at all-time instants. The central region vapor mole fraction for case-1 i.e. inner cavity filled case shows uniform and higher mole fraction for coaxial well-2 compared to coaxial well-1 at all-time instants due to smaller inner cavity radius. The average mole fraction for case-2 i.e. outer filled cavity case shows lower value at all time instants for coaxial well-2 due to higher rate of evaporation with time. In case-3, the average mole fraction for coaxial well-2 is higher at $t = 200$ (s) compared to coaxial well-1. This may be attributed to the greater role played by the vapor cloud interaction on evaporation rate for coaxial well-2 compared to that of co-axial well-1. Overall, Fig. 9 illustrates strong time dependence of evaporation process depending upon the design of coaxial well configuration.

3.3. Total evaporation rate

Fig. 10 compares the total evaporation rate from gravimetric and holographic measurement with the pure steady-state diffusion-limited evaporation rate for both the coaxial well configurations in the initial time period.

The evaporation rate from holographic measurement is in agreement with the gravimetric method for all test cases and for both coaxial well configurations. This confirms the accuracy of DHI technique for measurement of evaporation rate and vapor cloud concentration. Fig. 10 shows higher evaporation rate of co-axial well-1 compared to coaxial well-2 for all test cases. This is attributed to the higher cavity diameter and interfacial area for coaxial well-1 compared to coaxial well-2. The higher evaporation rate of coaxial well-1 is in conformity with the mole fraction results presented earlier in Figs. 6–8. The evaporation rate for Case-1 i.e filled inner cavity compares well with the diffusion limited evaporation rate. The evaporation rate from diffusion limited model shows lower value compared to the experimental evaporation rate for case-2 and case-3. The difference between actual evaporation rate and diffusion limited evaporation rate can be attributed to the greater role played by the convection process inside the vapor cloud.

The difference between experimental and diffusion-limited evaporation rate can be attributed to the convective contribution in evaporation rate (E_c). Grashof number (Gr) can be used as indication of strength of convection, which can be expressed as:

$$Gr = \frac{\rho_a.(\rho_{mix} - \rho_a) g R_m^{\,3}}{\mu_a^{\,2}} \tag{8}$$

$$(\rho_{mix} - \rho_a) = \frac{P_{sat}(T_{amb})(M_v - M_a)}{R_u T_{amb}} \tag{9}$$

Here, the mean radius of the cavity, $R_m = \frac{(R_i + R_o)}{2}$, where R_i is inner raduis and R_o is outer raduis. ρ_{mix} is the density of air-hexane vapor mixture. The Gr value for inner cavity is equal to 127 and 54 for coaxial well-1 and 2 respectively. Fig. 10 shows closer match of the evaporation rate from diffusion-limited model with experiments for coaxial well-2 due to the lower Grashof number. Hence, the convection effect on evaporation rate is negligible for smaller diameter cavity of the coaxial well. Dollet and Boulogne [41] reported greater role of convective flow on evaporation rate of circular disk of liquids for $Gr > 20$, for water evaporating from circular disk. In case of water, the density difference is positive, leading to a radially inward flow where unsaturated air is brought towards the center. The present case represents an opposite effect where a volatile heavy hydrocarbon is evaporating, and the sign of density difference is negative. Therefore, the nature of convective flow pattern is expected to be different with respect to Grashof number. As the mean radius of the cavities increases, Grashof number also increases. Grashof number values for the outer cavities of coaxial well-1 and coaxial well-2 are equal to 1014 and 428 respectively. This indicates increase in density difference induced radial outward flow and higher contribution of convective motion. This justifies the large difference between the diffusion limited and experimentally measured evaporation rate for case-2 as shown in Fig. 10.

In case-3, where liquid evaporates simultaneously from inner and outer cavities, the combined evaporation rate is lower than the sum of individual evaporation rate from the inner and outer cavity. The evaporation rate in case-3 is 24.5% and 35.18% lower compared to the sum of individual evaporation rate for coaxial well-1 and coaxial well- 2 respectively. For inner cavity, 25% and 35% decrease in global evaporation rate is observed in case-3 for coaxial well-1 and coaxial well-2, respectively. In outer cavity, global evaporation rate is reduced by 10% in coaxial well-1 and 17% in coaxial well-2. This can be attributed to the interaction between the vapor cloud from inner and outer well. These results correlate with vapor mole fraction results of case-3 discussed in previous section for both well configurations. It can be concluded that as the gap between the inner and outer coaxial cavity is

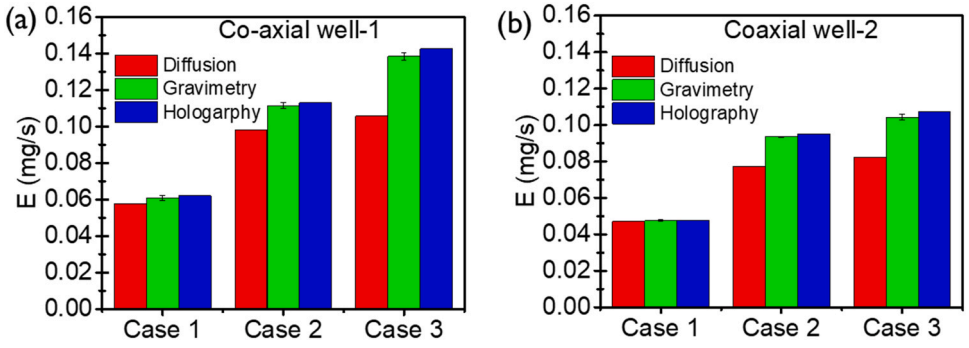

Fig. 10. Comparison of experimental (gravimetric and holographic) evaporation rate with steady state diffusion limited evaporation during initial time period for different test cases (Case 1, 2 and 3): (a) Coaxial well-1 and (b) Coaxial well-2.

reduced, the interaction of the two vapor cloud is stronger, which suppresses the evaporation rate of the coaxial cavities. The vapor cloud interaction is more prominent in the internal cavity than the outer cavity. This behavior can be helpful in the applications such as protein crystallization, microfluidic cell culture where suppression/control of evaporation rate from an evaporating microliter liquid body can be achieved with the help of another coaxial liquid body without any physical interaction.

3.4. Local evaporation rate and diffusive transport

Fig. 11 presents the local evaporation rate distributions from the holographic measurements for different test cases of coaxial well 1 and 2 to explain the average evaporation rate results of Fig. 10. The magnitude of local evaporation rate of inner and outer cavity in case-3 is lower than the evaporation rate from inner cavity of case-1 and outer cavity of case-2 respectively. This can be attributed to the restriction on radial vapor transport in the presence of vapor cloud from the neighboring cavity. Therefore, the change in gap between the cavity, not only influences the total evaporation rate but also the local evaporation rate. Similar observations have been made for the two droplet case, where strength of evaporation decreases when separation distance is reduced with reduction in strength of internal convection [17,18,20].

3.5. Interfacial temperature

IR thermography using a camera (Thermosensorik Model No: In-Sb 640 SM, 640 x 512 pixels, Pixel pitch: 15 μm x 15 μm, Wavelength: 1.1–5.3 μm) has been used to measure the interfacial temperature distribution of evaporating hexane inside the cavity. Since the emissivity of hexane is not known, the recorded IR signal cannot be accurately converted to temperature values. However, it can be helpful in comparing the relative difference in temperature along the interface between different test cases. We have assumed the emissivity to be equal to 1.0. Fig. 12 shows the temperature profile for coaxial well-1 during the initial time period (t = 0 + (s)). The experiments are conducted at the ambient temperature of 19 ± 0.5 °C and relative humidity of 60%.

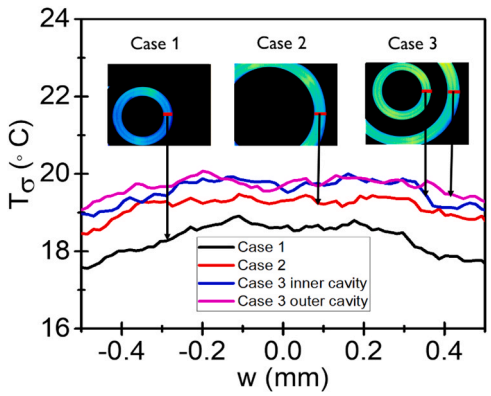

Fig. 12. Interfacial temperature distribution of the liquid interface of coaxial well-1 for different test cases (Case 1, 2 and 3) from IR thermography measurement at initial time period, t = 0 + (s). Here, w = (r−R_m) is the distance from the mid plane of the liquid filled cavity. IR thermograms are shown as inserts, where only the liquid interface area is shown, and remaining region are black.

The interfacial temperature distribution shows similar variation across the width of the cavity for all test cases i.e. the temperature reduces from the center of the cavity to its edge. Magnitude of average temperature for the case-3 is higher compared to that of cases 1 and 2. This may be attributed to lower evaporation rate for case 3 in comparison to case-1 and case-2 (see Fig. 11) resulting in lower evaporative cooling. Similarly, the average interfacial temperature for case-1 is lower than that of case-2. Higher evaporation flux in case-1 compared to case-2 observed in Fig. 11 supports the lower temperature observed in case-1 (Fig. 12). It may also be observed that the evaporation flux per unit area for case-1 and case-2 is respectively equal to 49.7 x 10^{-4} mg/s-mm^2 and 44.98 x 10^{-4} mg/s-mm^2 respectively (See Fig. 10), which also supports the interfacial temperature distribution of Fig. 12.

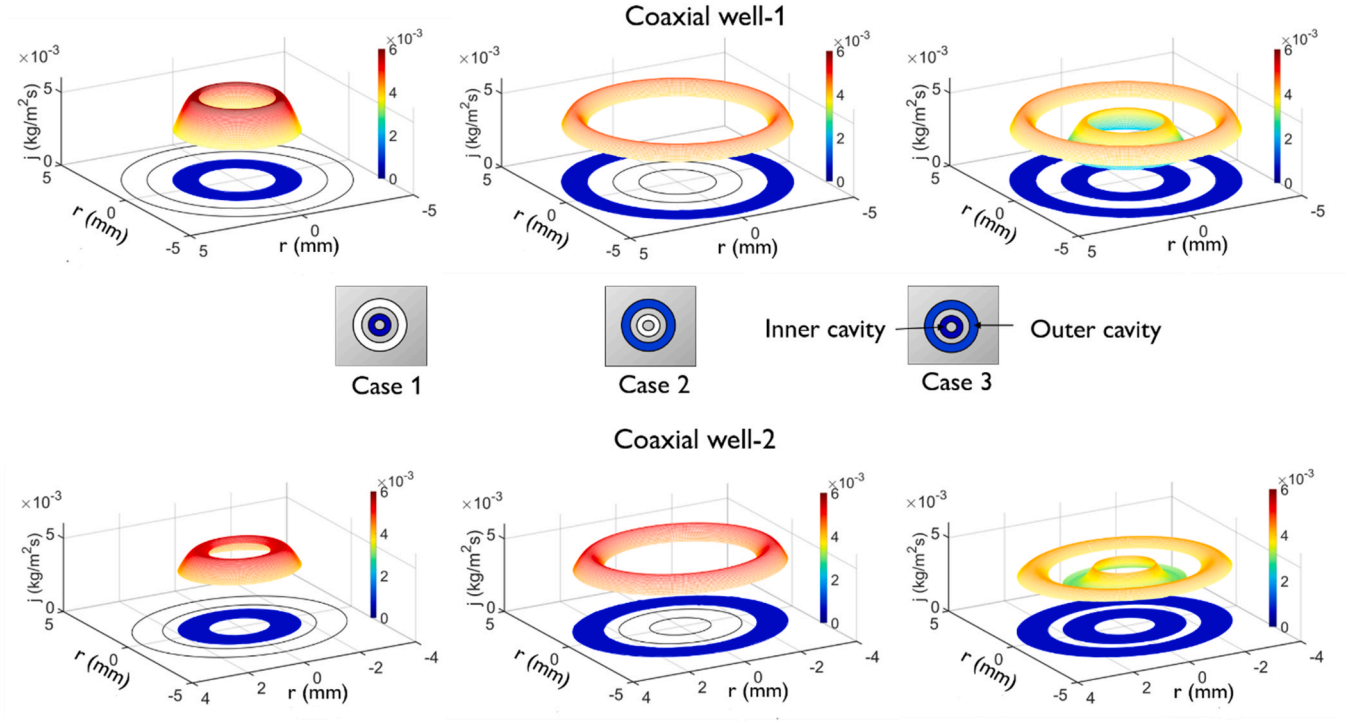

Fig. 11. Local evaporation rate (j) distribution for different test cases (Case 1, 2 and 3) of Coaxial well-1 (a–c) and coaxial well-2 (d–f).

4. Conclusions

The present study investigates the interaction of vapor cloud from evaporation of two coaxial cavities. The evaporation of high molecular weight liquid hydrocarbon, hexane evaporating from a micro-litter volume coaxial well is studied using digital holographic Interferometry. Gravimetric measurements have been carried out to measure the evaporation rate and confirm the accuracy of holographic interferometry technique and tomographic reconstruction process. The IR thermography measurements are carried out to explain the local evaporation rate distribution by correlating with the evaporation induced cooling. Diffusion limited simulation study using Comsol Multiphysics software has been carried out to quantify the role of convection on mass transfer process. The interaction of vapor cloud from evaporation of two coaxial cavities is studied by varying the separation distance or gap between the coaxial cavities. Important summary of findings from the present study are as follows:

- Average evaporation rate from inner and outer cavity of coaxial well with both cavities filled with liquid reduces in comparison to the case when liquid is evaporating from individual cavities. There is a decrease in evaporation rate of about 30% for the inner cavity when both inner and outer cavities are filled in comparison to when only the inner cavity is filled with liquid. The decrease in evaporation rate depends on the gap or separation distance between the two coaxial cavities. The interaction between vapor cloud from individual cavity influences the local evaporation rate.
- The diffusion limited evaporation rate from simulation study matches well with the experimental evaporation rate from digital holography and gravimetry at low Grashof number. The mismatch increases with increase in Grashof number.
- The temperature drop of the liquid interface due to evaporative cooling correlates well with the local evaporation rate from digital holography analysis. The temperature drop is lower when both inner and outer cavities are filled with liquid compared to when evaporation takes place from individual cavity.
- The control of evaporation rate from individual cavities in coaxial well configuration by adjusting the gap or separation distance between cavities can be used as a design parameter in several applications i.e. protein crystallization, microfluidic cell culture and micro manufacturing for optimal performance.

CRediT authorship contribution statement

Digvijay Shukla: Data acquisition, Data analysis, Writing – original draft. **Pradipta K. Panigrahi:** Conceptualization, Supervision, Writing – review & editing.

Declaration of Competing Interest

The authors declare that they have no known competing financial interests or personal relationships that could have appeared to influence the work reported in this paper.

Acknowledgments

Authors acknowledge the support from Ministry of Electronics and Information Technology, Government of India.

References

[1] S. Halldorsson, E. Lucumi, R. Gómez-Sjöberg, R.M. Fleming, Advantages and challenges of microfluidic cell culture in polydimethylsiloxane devices, Biosens. Bioelectron. 63 (2015) 218–231.
[2] V. Dugas, J. Broutin, E. Souteyrand, Droplet evaporation study applied to DNA chip manufacturing, Langmuir 21 (2005) 9130–9136.
[3] J. Jing, J. Reed, J. Huang, X. Hu, V. Clarke, J. Edington, D. Housman, T. S. Anantharaman, E.J. Huff, B. Mishra, Automated high resolution optical mapping using arrayed, fluid-fixed DNA molecules, Proc. Natl. Acad. Sci. USA 95 (1998) 8046–8051.
[4] K.S. Elvira, X.C. i Solvas, R.C. Wootton, A.J. Demello, The past, present and potential for microfluidic reactor technology in chemical synthesis, Nat. Chem. 5 (2013) 905–915.
[5] C. Situma, M. Hashimoto, S.A. Soper, Merging microfluidics with microarray-based bioassays, Biomol. Eng. 23 (2006) 213–231.
[6] A. Walzl, N. Kramer, M.R. Mazza, D. Falkenhagen, M. Hengstschläger, D. Schwanzer-Pfeiffer, H. Dolznig, A simple and cost efficient method to avoid unequal evaporation in cellular screening assays, which restores cellular metabolic activity, Int. J. Appl. Sci. Technol. 2 (2012).
[7] T.K. Pradhan, P.K. Panigrahi, Suppressing internal convection of a droplet using confinement during protein crystallization, J. Appl. Phys. 128 (2020), 084701.
[8] C.T. Chen, F.G. Tseng, C.C. Chieng, Evaporation evolution of volatile liquid droplets in nanoliter well array, in: The 13th International Conference on Solid-State Sensors, Actuators and Microsystems, 2005, Digest of Technical Papers, Transducers'05, IEEE, 2005, pp. 812–815.
[9] A.P. Mouat, C.E. Wood, J.E. Pye, J.C. Burton, Liquid deposition through evaporation, Phys. Rev. Fluids 4 (2019), 100512.
[10] H. Hoffman, R. Sijs, T. de Goede, D. Bonn, Controlling droplet deposition with surfactants, Phys. Rev. Fluids 6 (2021), 033601.
[11] T.K. Pradhan, P.K. Panigrahi, Deposition pattern of interacting droplets, Colloids Surf. A: Physicochem. Eng. Asp. 482 (2015) 562–567.
[12] S.K. Saroj, P.K. Panigrahi, Drying pattern and evaporation dynamics of sessile ferrofluid droplet on a PDMS substrate, Colloids Surf. A: Physicochem. Eng. Asp. 580 (2019), 123672.
[13] T.K. Pradhan, P.K. Panigrahi, Evaporation induced natural convection inside a droplet of aqueous solution placed on a superhydrophobic surface, Colloids Surf. A: Physicochem. Eng. Asp. 530 (2017) 1–12.
[14] C.T. Chen, F.G. Tseng, C.C. Chieng, Evaporation evolution of volatile liquid droplets in nanoliter wells, Sens. Actuators A: Phys. 130 (2006) 12–19.
[15] N.S. Lynn, C.S. Henry, D.S. Dandy, Evaporation from microreservoirs, Lab Chip 9 (2009) 1780–1788.
[16] D. Shukla, P.K. Panigarhi, Digital holographic interferometry investigation of liquid hydrocarbon vapor cloud above a circular well, Appl. Opt. 59 (2020) 5851–5863.
[17] T.K. Pradhan, P.K. Panigrahi, Influence of an adjacent droplet on fluid convection inside an evaporating droplet of binary mixture, Colloids Surf. A: Physicochem. Eng. Asp. 500 (2016) 154–165.
[18] T.K. Pradhan, P.K. Panigrahi, Hydrodynamics of two interacting liquid droplets of aqueous solution inside a microchannel, Langmuir 34 (2018) 4626–4633.
[19] T.K. Pradhan, P.K. Panigrahi, Vapor mediated interaction of two condensing droplets, Colloids Surf. A: Physicochem. Eng. Asp. 608 (2021), 125555.
[20] Y. Wen, P.Y. Kim, S. Shi, D. Wang, X. Man, M. Doi, T.P. Russell, Vapor-induced motion of two pure liquid droplets, Soft Matter 15 (2019) 2135–2139.
[21] R. Bazile, D. Stepowski, Measurements of vaporized and liquid fuel concentration fields in a burning spray jet of acetone using planar laser induced fluorescence, Exp. Fluids 20 (1995) 1–9.
[22] A. Charogiannis, F. Beyrau, Laser induced phosphorescence imaging for the investigation of evaporating liquid flows, Exp. Fluids 54 (2013) 1518.
[23] P. Kelly-Zion, C.J. Pursell, N. Hasbamrer, B. Cardozo, K. Gaughan, K. Nickels, Vapor distribution above an evaporating sessile drop, Int. J. Heat. Mass Transf. 65 (2013) 165–172.
[24] R. O'Brien, P. Saville, Investigation of liquid drop evaporation by laser interferometry, Langmuir 3 (1987) 41–45.
[25] G. Toker, J. Stricker, Holographic study of suspended vaporizing volatile liquid droplets in still air, Int. J. Heat. Mass Transf. 39 (1996) 3475–3482.
[26] S. Dehaeck, A. Rednikov, P. Colinet, Vapor-based interferometric measurement of local evaporation rate and interfacial temperature of evaporating droplets, Langmuir 30 (2014) 2002–2008.
[27] H. Hu, R.G. Larson, Evaporation of a sessile droplet on a substrate, J. Phys. Chem. B 106 (2002) 1334–1344.
[28] P. Kelly-Zion, C. Pursell, S. Vaidya, J. Batra, Evaporation of sessile drops under combined diffusion and natural convection, Colloids Surf. A: Physicochem. Eng. Asp. 381 (2011) 31–36.
[29] P.L. Kelly-Zion, C.J. Pursell, R.S. Booth, A.N. VanTilburg, Evaporation rates of pure hydrocarbon liquids under the influences of natural convection and diffusion, Int. J. Heat. Mass Transf. 52 (2009) 3305–3313.
[30] P.F. Linstrom, W. Mallard, NIST Chemistry, WebBook-SRD, 2001.
[31] K. Beverley, J. Clint, P.I. Fletcher, Evaporation rates of pure liquids measured using a gravimetric technique, Phys. Chem. Chem. Phys. 1 (1999) 149–153.
[32] C.B. Willingham, W.J. Taylor, J.M. Pignocco, F.D. Rossini, Vapor pressures and boiling points of some paraffin, alkylcyclopentane, alkylcyclohexane, and alkylbenzene hydrocarbons, J. Res. Natl. Bur. Stand. 35 (1945) 219–244.
[33] M. Takeda, H. Ina, S. Kobayashi, Fourier-transform method of fringe-pattern analysis for computer-based topography and interferometry, JOSA 72 (1982) 156–160.
[34] R.M. Goldstein, H.A. Zebker, C.L. Werner, Satellite radar interferometry: two-dimensional phase unwrapping, Radio Sci. 23 (1988) 713–720.
[35] C.J. Dasch, One-dimensional tomography: a comparison of Abel, onion-peeling, and filtered backprojection methods, Appl. Opt. 31 (1992) 1146–1152.
[36] S. Ma, H. Gao, L. Wu, Modified Fourier-Hankel method based on analysis of errors in Abel inversion using Fourier transform techniques, Appl. Opt. 47 (2008) 1350–1357.

[37] H. Chehouani, A simple Abel inversion method of interferometric data for temperature measurement in axisymmetric medium, Opt. Lasers Eng. 50 (2012) 336–344.
[38] L. Pendrill, Refractometry and gas density, Metrologia 41 (2004) S40–S51.
[39] A. Börzsönyi, Z. Heiner, M. Kalashnikov, A. Kovács, K. Osvay, Dispersion measurement of inert gases and gas mixtures at 800 nm, Appl. Opt. 47 (2008) 4856–4863.
[40] W. Gardiner Jr., Y. Hidaka, T. Tanzawa, Refractivity of combustion gases, Combust. Flame 40 (1981) 213–219.
[41] B. Dollet, F. Boulogne, Natural convection above circular disks of evaporating liquids, Phys. Rev. Fluids 2 (2017), 053501.